Geophysical Journal International

Geophys. J. Int. (2023) **235,** 312–325
Advance Access publication 2023 May 25
GJI Seismology

https://doi.org/10.1093/gji/ggad221

Fast migration episodes within earthquake swarms

Tomáš Fischer [1], Sebastian Hainzl[2] and Josef Vlček[1]

[1]*Faculty of Science, Charles University, Prague, Czechia. E-mail: fischer@natur.cuni.cz*
[2]*GFZ German Research Centre for Geosciences, Potsdam, Germany*

Accepted 2023 May 17. Received 2023 May 2; in original form 2022 December 19

SUMMARY

The hypocentres of natural earthquake swarms and injection-induced seismicity usually show systematic migration, which is considered to be a manifestation of their triggering mechanism. In many of these cases, the overall growth of the earthquake distribution is accompanied by short episodes of rapid migration, the origin of which is still not sufficiently clarified. We review the possible triggering mechanisms of these migrating episodes and propose a graphical method for distinguishing internal and external triggering forces. We also analyse the theoretical relationship between the evolution of the cumulative seismic moment and the rupture area and propose two models, the crack model and the rupture front model, which can explain the spreading of hypocentres. We developed an automatic algorithm for detecting fast migration episodes in seismicity data and applied it to relocated catalogues of natural earthquake swarms in California, West Bohemia, and Iceland, and to injection-induced seismicity. Fast migration episodes is shown to be relatively frequent during earthquake swarms (8–20 per cent of all events) compared to fluid-induced seismicity (less than 5 per cent of the events). Although the migration episodes were detected independently of time, they grew monotonically with time and square-root dependence of radius on time was found suitable for majority of sequences. The migration velocity of the episodes of the order of 1 $m\,s^{-1}$ was found and it anticorrelated with their duration, which results in a similar final size of the clusters scattering around 1–2 km. Comparison of seismic moment growth and activated fault area with the predictions of the proposed models shows that both the rupture front model and the crack model are able to explain the observed migration and that the front model is more consistent with the data. Relatively low estimated stress drops in the range of 100 Pa to 1 MPa suggest that aseismic processes are also responsible for cluster growth. Our results show that the fast migrating episodes can be driven by stress transfer between adjacent events with the support of aseismic slip or fluid flow due to dynamic pore creation.

Key words: Earthquake source observations; Statistical seismology; Earthquake interaction; Seismicity migration.

1 INTRODUCTION

Migration of hypocentres is a common attribute of induced injection seismicity and earthquake swarms, which usually distinguishes them from aftershock sequences. It is likely related to aseismic driving mechanisms, such as fluid intrusions or aseismic slip.

Migration of swarms in various tectonic environments is attributed to fluid or magma migration, for example in Iceland (Woods *et al.* 2019; Fischer *et al.* 2022), Japan (Yoshida & Hasegawa 2018a), (Yoshida & Hasegawa 2018b; Guo *et al.* 2023), Afar Rift (Wright *et al.* 2012), Yellowstone (Shelly & Hill 2011; Massin *et al.* 2013) or West Bohemia/Vogtland (Bachura *et al.* 2021). Different migration scenarios are observed from monotonous migration in the horizontal or vertical direction or migration with direction changes within the evolution of the seismic cluster. The shape of the spreading envelope however depends also on the initial fault criticality (De Barros *et al.* 2021). In contrast to direct influence of pore pressure perturbation, aseismic slip is able to explain fast hypocentre migration (Lohman & McGuire 2007).

Earthquake migration patterns, however, often exhibit not only spreading envelopes but also fast-growing episodes embedded in the overall migration trend. This was observed for the 2009 Long Valley Caldera swarm (Shelly & Hill 2011), Yellowstone 2008–2009 swarm (Massin *et al.* 2013), Greece swarms (Kapetanidis & Deschamps 2015; De Barros *et al.* 2020; Dublanchet & De Barros 2020) and West Bohemia swarms (Fischer & Hainzl 2021). Similar fast migration patterns are also observed during tremor activity (Ghosh *et al.* 2010; Gombert & Hawthorne 2023). It is not the

absolute speed of migration that identifies fast migration episodes. Rather, they are characterized by their occurrence behind the overall migration envelope and by a migration velocity higher than the envelope migration speed. As shown in Fig. 1, it also turns out that when distance–event index plots are used instead of distance–time plots, the originally nonlinear and interrupted migration front becomes more linear and continuous. This is consistent with a front-rupture model where new ruptures are triggered at the edge of the rupture zone due to stress transfers from previous earthquakes and fluid flow enabled by increased permeability in the rupture zone (Fischer & Hainzl 2021).

In this paper, we focus on the analysis of the fast migration episodes. Their features and physics are not well studied so far. For that purpose, we first discuss the possible seismic and aseismic driving mechanisms and present two end-member models, the crack-type and front-type model and their predictions of the cumulative seismic moment and activated area by the ruptures. Furthermore, we developed a fully automatic procedure based on the distance–index information to detect significant migration features in earthquake data without assuming any specific time dependence. The new detection algorithm is then applied to selected swarms from California, Iceland and West Bohemia, as well as injection-induced seismicity. We systematically characterize their frequency, timing, spatial spreading and moment release and compare their pattern with the different expectations for crack-type and front-type growth models. Our results provide new insights into the patterns of fast migration episodes, which help us to understand the underlying physics.

2 EARTHQUAKE MIGRATION

2.1 Possible sources of earthquake migration

The driving force of earthquake migration can be of external or internal origin (Shapiro *et al.* 1997; Yamashita 1999; Parotidis *et al.* 2003; Fischer & Hainzl 2021).

In the case of *external* (aseismic) origin of the driving force, the seismicity growth is controlled by an aseismic time-dependent driving mechanism, which triggers the observed seismicity. In this case, fluid injection or aseismic slip are candidates for the driving force. These mechanisms are usually modelled by a time-dependent process (pore pressure diffusion, hydraulic fracture growth, transient creep and similar). In particular, the pore pressure diffusion model assumes that earthquakes map the advance of the pore pressure front. We assume a homogeneous ambient stress field and medium with constant diffusivity of the rock, where the permeability and pore pressure field are not altered by seismic rupturing and related stress changes. In that case, the distance r of the propagating pore pressure front from the pressure source grows as $r = \sqrt{4\pi Dt}$ (Shapiro *et al.* 1997). Here, t is the time from the first contact of the pore pressure source with the host rock, and D is the hydraulic diffusivity. Alternatively, hydraulic fractures can be an aseismic driving source for the observed seismicity. In a simplistic model, the hydraulic fracture growth is determined by the mass conservation of the injected fluid. Provided a constant injection rate, the relation between the triggering front distance r and time t depends on the fracture geometry. If the thickness of the hydraulic fracture is constant, r depends linearly on t for 1-D fracture propagation. Similarly, r grows with the square root of time for unlimited 2-D hydrofracture fracture propagation (Fischer *et al.* 2008, 2009). Finally, aseismically expanding creep on faults (slow slip) might trigger earthquakes with migrating patterns due to the (constant) propagation of the slip front (Passarelli *et al.* 2021).

In the case of *internal* (seismic) origin of the driving force, the seismicity growth is controlled by the earthquake ruptures themselves. Such a self-driven process can explain aftershock sequences and also fast migrating episodes as discussed below. Earthquake ruptures create pore space and damage on and in the surrounding of the rupture (Marone *et al.* 1990; Yamashita 1999), as well as dynamic and static coseismic stress changes. The intensity of the stress changes is the highest on the front of the rupture tip. Thus, a new rupture most likely nucleates adjacent to the previous one, assuming homogeneous medium properties and pre-stress. The underlying processes are not necessarily continuous in time because strength heterogeneities combined with the delayed rupturing of barriers due to stress corrosion might lead to a broad distribution of waiting times (also called interevent times). For example, the interevent times of the swarms in NW Bohemia show a power-law distribution related to a strong sub-clustering in the swarm activity (Hainzl & Fischer 2002). Accordingly, no clear time dependence of seismicity is expected.

2.2 Graphical analysis

Migration patterns are usually analysed in the coordinate–time (x–t) domain (Fig. 1a), where the time t is used as the independent variable. However, this postulates that time controls the seismogenic process. Such plots are suitable to identify and characterize the external aseismic driving force, for example to estimate the hydraulic diffusivity D in the case of seismicity driven by pore-pressure diffusion.

Additionally to time, the event order can be used as the independent variable, which is also termed natural time (Rundle *et al.* 2018). In such a case, a coordinate-event-index (x–N) plot is produced (Fig. 1b). This approach postulates that the seismic ruptures control the evolution of the seismicity, that is the process is self-driven. Exploring the seismicity spreading dependent on the event order ignores the influence of time on the seismicity and can facilitate the investigation of self-driven cluster formations.

The different representation of seismicity migration using x–t and x–N plots is apparent in Fig. 1 of this paper and fig. 1 in Fischer & Hainzl (2021). In the x–N plot, the periods of quiescence disappear, and the original temporal clusters found in the x–t plot merge into a continuous seismicity sequence migrating in a single dominating direction. Most triggering fronts seem to show a linear envelope whose slope (migration velocity measured in metres per event) stays almost constant for longer periods. Fig. 1 also illustrates the two phenomena mentioned above: the overall growth of the seismic clouds is manifested in the triggering front envelope and the embedded rapid episodes that propagate both in the same and opposite directions as the triggering envelope.

A combined analysis of both x–t and x–N plots helps us to understand the processes in more detail. It can be used to indicate the aseismic driving mechanisms and self-driven processes. The general procedure is illustrated in the flow diagram in Fig. 2. To explain the strength of the combined analysis, we analysed synthetic simulations of seismicity driven by pore-pressure and self-driven rupture propagation (Appendix B1). While the growth pattern of the externally (aseismically) driven seismicity is continuous in the x–t plot (and also in the x–N plot), we find that internally driven seismicity (self-driven) shows a continuous growth only in the x–N

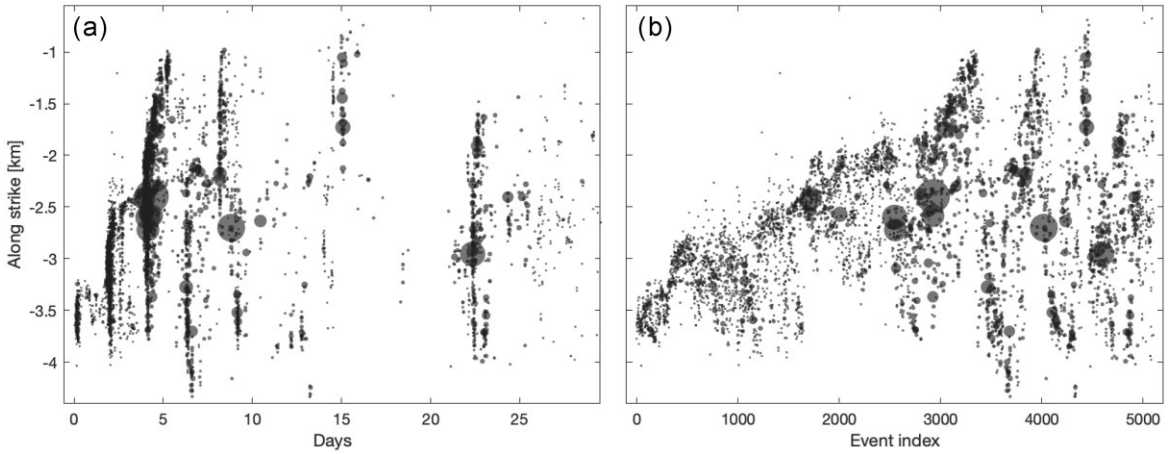

Figure 1. Migration of the earthquakes in the West Bohemia seismic swarm occurred in 2008: (a) coordinate-time and (b) coordinate-event-index plot. Note the episodic occurrence of activity in the coordinate-time plot compared to the overall continuous spreading of activity in the coordinate-event-index plot. The size of symbols scales with event magnitude ranging from −1 to 3.5.

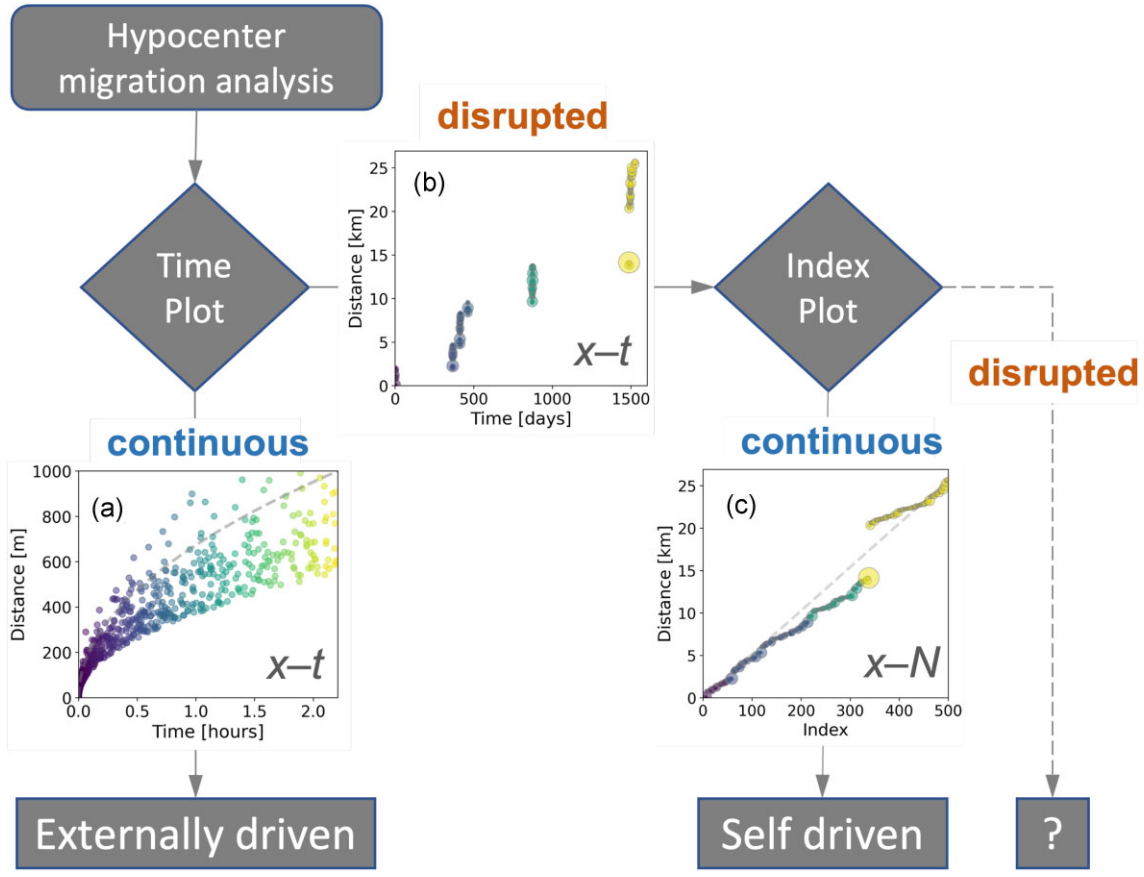

Figure 2. Flow diagram for identification of the background driving mechanism using coordinate–time (x–t) and coordinate–index (x–N) plot. The diagrams show simulations of seismicity growth using the pore pressure diffusion model (A) and front migration model (B and C); see more details in the Appendix B.

plot, but a disrupted growth in the x–t plot. This observation allows, in the first approximation, to visually distinguish the different types of driving forces (Fig. 2). It should be noted that transient catalogue incompleteness in the form of occasional missing events can also lead to discontinuous event migration in the x–N plot, similar to that seen in Fig. 2(c) caused by the largest rupture in the sequence.

3 CHARACTERIZATION OF SELF-DRIVEN SEISMICITY

The growth of self-driven seismicity can be understood by different models predicting the growth of the activated area. Among them, we discuss the two following end-member cases, that is, the *crack* and the *front model* (Fig. 3).

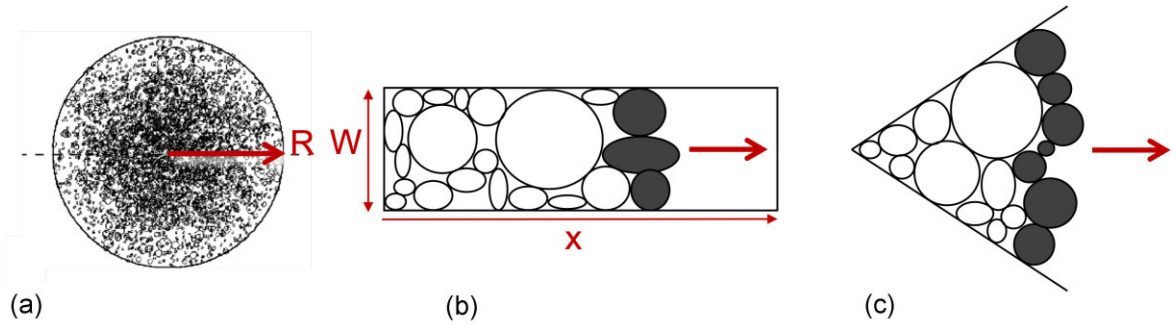

Figure 3. Schematic illustration of the seismicity growth in the (a) *crack* and *front model* in the case of the channel (b) and wedge (c) growth.

The *crack model* is based on the effective stress drop approach (Madariaga & Ruiz 2016; Fischer & Hainzl 2017). It supposes that a crack can be replaced by a cluster of events, which releases the total stress. Depending on the fault rheology, stress is released and reloaded either by re-rupturing of asperities (brittle rheology) or by a combination of seismic and seismically triggered aseismic slip. The effective (seismic) stress drop is found to be small in the case of a large contribution of creep to the slip (ductile rheology). The *crack model* assumes ongoing slip within the rupture area. In contrast, seismicity is assumed to be only triggered at the crack tip in the case of the *front model*. Note that the latter is equivalent to the pulse model for concentrated slip on the rupture front during a single earthquake rupture (Heaton 1990). As discussed by Fischer & Hainzl (2021), the front model explains observed linear or square-root event migration patterns observed in the *x*–*N* plot.

3.1 Seismic moment release versus activated area

In the following, we investigate the relationship between the activated area of the fault segment and the total seismic moment released during an episode. For this purpose, we consider the crack solution of a single earthquake. In particular, we use the relation between the rupture area A and the seismic moment M_0 of an earthquake (see e.g. review of Madariaga & Ruiz 2016),

$$A = \left(\frac{M_0}{f\,\Delta\sigma}\right)^{2/3} \tag{1}$$

with $\Delta\sigma$ being the static stress drop and the geometric constant $f = \frac{16}{7}\pi^{-3/2}$ for a circular rupture.

In the case of the *crack model*, the fault segment consists of densely distributed asperities that rupture, reload and re-rupture individually until the stress is released everywhere within the rupture area, leading to the highest event density in the central part of the fault segment. The summed area of individual ruptures exceeds the area of the activated fault segment, and is related to the cumulative seismic moment of the swarm activity according to

$$A_{\text{crack}} = \left(\frac{\sum M_{0,i}}{f\,\Delta\sigma}\right)^{2/3}, \tag{2}$$

where $\Delta\sigma$ represents the effective stress drop (Fischer & Hainzl 2017).

In the case of the *front model*, re-rupturing of asperities does not occur, and each rupture increases the total rupture area of the earthquake sequence. This can happen if the earthquake–earthquake interactions are mediated by afterslip in the vicinity of the asperities and thus the stress increases due to neighbouring rupture are small compared to earthquake stress drops, preventing reloading of already ruptured asperities. Thus a front migration might be facilitated by aseismic processes within the ruptured area, such as an aseismic slip or fluid flow due to dynamic pore creation as proposed by Yamashita (1999). On a fault plane, two geometrical concepts were considered by Fischer & Hainzl (2021): the channel model describing a unilateral growth along a channel of width W and the sector model describing a 2-D sectorial growth with angle θ (Figs 3b and c). In the case of the *front model*, because the ruptures do not overlap, the sum of areas of individual ruptures A_i fits the area of the activated fault segment. By expressing A_i using eq. (1), the total area is

$$A_{\text{front}} = \Sigma A_i = \sum \left(\frac{M_{0,i}}{f\,\Delta\sigma}\right)^{2/3} = \left(\frac{\left(\sum M_{0,i}^{2/3}\right)^{3/2}}{f\,\Delta\sigma}\right)^{2/3}, \tag{3}$$

where $\Delta\sigma$ refers to the static stress drop of the earthquakes, and the final rearrangement is aimed at obtaining the same form as in eq. (2). Hence eqs (2) and (3) are similar in the form

$$A = \left(\frac{M_0^T}{f\,\Delta\sigma}\right)^{2/3}, \tag{4}$$

where the seismic moment is replaced by

$$M_0^T \equiv \sum M_{0,i} \qquad \text{Crack model} \tag{5a}$$

$$\equiv \left(\sum M_{0,i}^{2/3}\right)^{3/2} \qquad \text{Front model} \tag{5b}$$

Thus, plotting M_0^T versus empirically estimated rupture area A in a double-logarithmic scale should show a linear slope with a gradient of 1.5 and an offset related to $f\Delta\sigma$. The comparison of the fits of both eqs (5a) and (5b) can point to the possible character of the analysed episode - a crack- or front-type migration.

For comparison, we also analyse the relationship between the activated area S and total seismic moment M_0^T within a sequence for the pore pressure diffusion model. In this case, the number of earthquakes, and thus the cumulative seismic moment, is proportional to the injected volume, assuming a homogeneous medium and pre-stress. In the case of a constant injection rate q and 2-D diffusion, both the area enclosed by the fluid front at radius $\sqrt{4\pi\,Dt}$ and the volume, $Q = qt$, grow linearly with time. Then, the cumulative seismic moment is proportional to the injected volume (McGarr 2014) and consequently to the activated area

$$M_0^T = \sum M_{0,i} = m\,A \qquad \text{Diffusion model,} \tag{6}$$

where m defines the mean seismic moment density. In a double-logarithmic scale, this relation corresponds to a linear slope with a gradient of 1.0 and an offset m.

Table 1. Total number of events per data set, their depth range, duration of the activity, magnitude range of the seismicity and estimated completeness magnitudes M_c using the Maximum Curvature (MaxC) method.

Swarm	Number of events	Depth (km)	Duration (d)	Magnitudes	M_c
West Bohemia (2000)	5104	6.5–10.4	156	−0.3–3.0	0.2
West Bohemia (2008)	3891	6.0–10.3	117	−1.0–3.5	−0.1
West Bohemia (2011)	9496	6.8–10.2	31	0.0–3.6	0.2
West Bohemia (2014)	2824	6.9–11.0	103	−1.0–4.4	−0.1
West Bohemia (2018)	3424	6.0–11.0	15	0.5–3.8	0.6
LongValleyCaldera	4580	4.0–8.0	154	−1.0–3.5	−0.2
Iceland, Reykjanes	9000	2.0–6.0	23	0.0–5.3	1.9
Basel	1974	3.6–4.9	8	0.1–3.4	0.8
Soultz (2000)	5030	3.8–5.5	10	−0.9–2.5	0.1
Soultz (2003)	1675	3.6–5.7	46	−0.5–2.9	0.0
Helsinki	6121	4.6–6.3	60	−1.9–1.2	−0.3

4 ANALYSIS OF THE FAST MIGRATION EPISODES

4.1 Data

We analysed two different types of seismic catalogues—natural earthquake swarms observed in West Bohemia (Czech Republic), Iceland and California (USA) and injection-induced seismicity recorded during stimulation of deep geothermal projects—Soultz-sous-Forets (France), Basel (Switzerland) and Helsinki (Finland) (Table 1). West Bohemia is a well-known area for its repeated seismic activity, where many earthquake swarms were instrumentally recorded by the local seismic network Webnet since the 1990s. In this study, relocated swarms from the years 2000, 2008, 2011, 2014 and 2018 (Bachura *et al.* 2021) are used for further analysis. Additionally, we analyse a very similar seismic activity from Iceland, where earthquake swarms on Reykjanes peninsula (SW of Iceland) were recorded by a local seismic network. Specifically, we investigate the 2021 swarm preceding the eruption of the Fagradasfjall volcano (Fischer *et al.* 2022). The last natural swarm data set is from Long Valley Caldera, California, recorded in 2014 (Shelly *et al.* 2016).

The second data type comes from hydraulic injections in deep geothermal projects. The first part of these data sets consist of stimulations of two different wells at Soultz-sous-Forets in the years 2000 and 2003 (Charléty *et al.* 2009). Another induced-seismicity case stems from the Basel stimulation in 2008 (Kraft & Deichmann 2014). The final and newest used data set is from the Helsinki geothermal site where in year 2020 near-real time processing during stimulation was performed in order to lower the risk of strong earthquakes (Kwiatek *et al.* 2022a, b).

4.2 Detection of the fast migration episodes

To detect migration pattern within those swarm data, we developed an automatic migration detection algorithm, described in detail in the Appendix A. The algorithm aims to detect systematic increases in the distances of subsequent events relative to the location of an earthquake in the sequence. In particular, it is based on the distances' rank variability. Only the fact counts whether one event occurred closer or farther away, and neither their time difference nor the absolute distances are considered. Thus, by its construction, the algorithm does not make any assumptions about the specific space–time relations of the underlying process.

Migration patterns are usually observable in the whole magnitude range. Thus we use all recorded earthquakes in the catalogue for the analysis. The changes of magnitude of completeness may affect the total seismic moment; this influence can be however neglected because of only tiny contribution of the smallest events to the total seismic moment. To address the possible influence, in the supplementary material, we also show results for all data sets, using only earthquakes with magnitudes above the estimated completeness magnitude.

Using our detection algorithm (see Appendix A), we detected 480 different migration episodes consisting of 7725 earthquakes in total. The detected events are colour-coded in Figs 4 and 5, showing the projected hypocentres on the fitted fault planes in the case of all analysed swarms, except the Iceland case which has no planar structure. While Figs 4 and 5 show the events as a function of the earthquake index, Figs S1 and S2 of the supplementary material show the same as a function of time. Note that the migration episodes were detected by the automatic algorithm using hypocentral distances rather than projected on a plane. Nevertheless, the detected episodes form, either in one or even both fault dimensions, mostly connected clusters with rare gaps between subsequent events. For four examples, Fig. 6 shows the distance versus time and the hypocentre projections on the fault planes, where the time is colour-coded.

To check whether the detected events may be aftershocks of a main shock in the first phase of the cluster, we calculated for each episode the ratio between the seismic moment release of the first half of the events and that of the second half of events. Fig. 7 shows that the ratio scatters around one, indicating that magnitudes occur rather randomly within the sequence, typical for swarms rather than main shock–aftershock sequences. This is confirmed by the observation that only 9 per cent of the detected episodes started with the largest event. Similar results are obtained for the analysis restricted to events with a magnitude above the completeness magnitude (see Supplementary Fig. S6).

4.3 Analysis of detected migration episodes

We first analysed the detected episodes according to the following research questions.

4.3.1 How frequent are those episodes within the swarm activity?

To answer this question, we calculated the ratio between the number of events within all detected episodes and the total number of earthquakes in each swarm.

To compare the results, we tested synthetic sequences without any systematic migration. In particular, we analysed 100 sequences

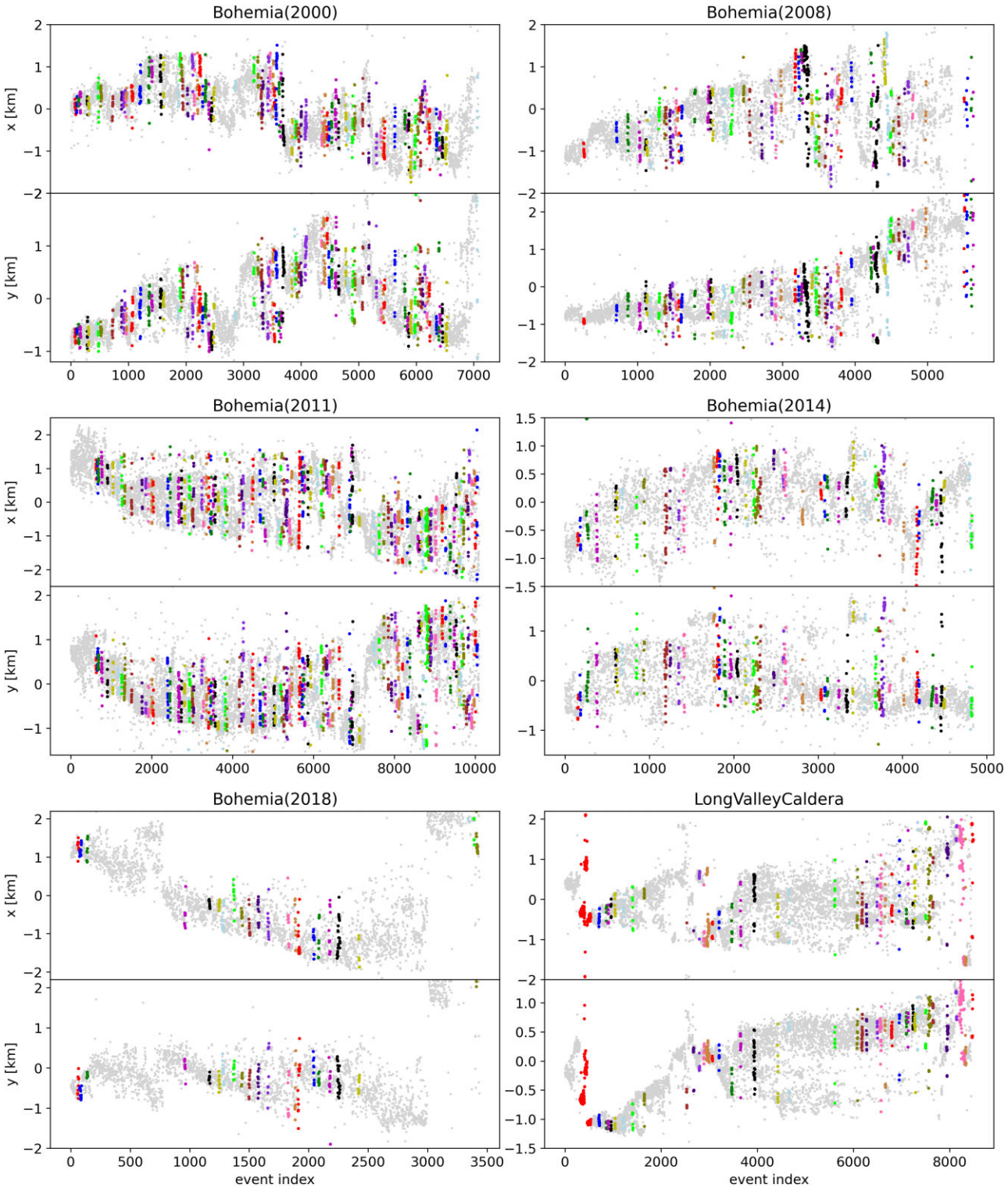

Figure 4. Identified clusters with migration patterns in the analysed natural swarms, except the Iceland case which has no planar structure. The name of each data set is marked as title, while the coordinates on the corresponding fault plane are shown as a function of the event index for each case; x and y denote to the along strike and along dip directions. For comparison, the time dependence of the coordinates (x–t plots) is shown in Supplementary Fig. S1.

of 5000 events uniformly distributed within a box with a 5 km × 5 km dimension (Poisson process). To be more realistic, we also run simulations of the Epidemic Type Aftershock Sequence (ETAS) model (Ogata 1998), which considers aftershocks triggered by the background activity. Details are provided in the Appendix B2.

The resulting ratio of clustered events with the overall swarm activity varies strongly between the analysed data sets. As shown in Fig. 8, the ratio is highest in the natural swarms observed in Western Bohemia, Long Valley Caldera and Iceland. It decreases from 20 per cent to 8 per cent with time for the Western Bohemian swarms

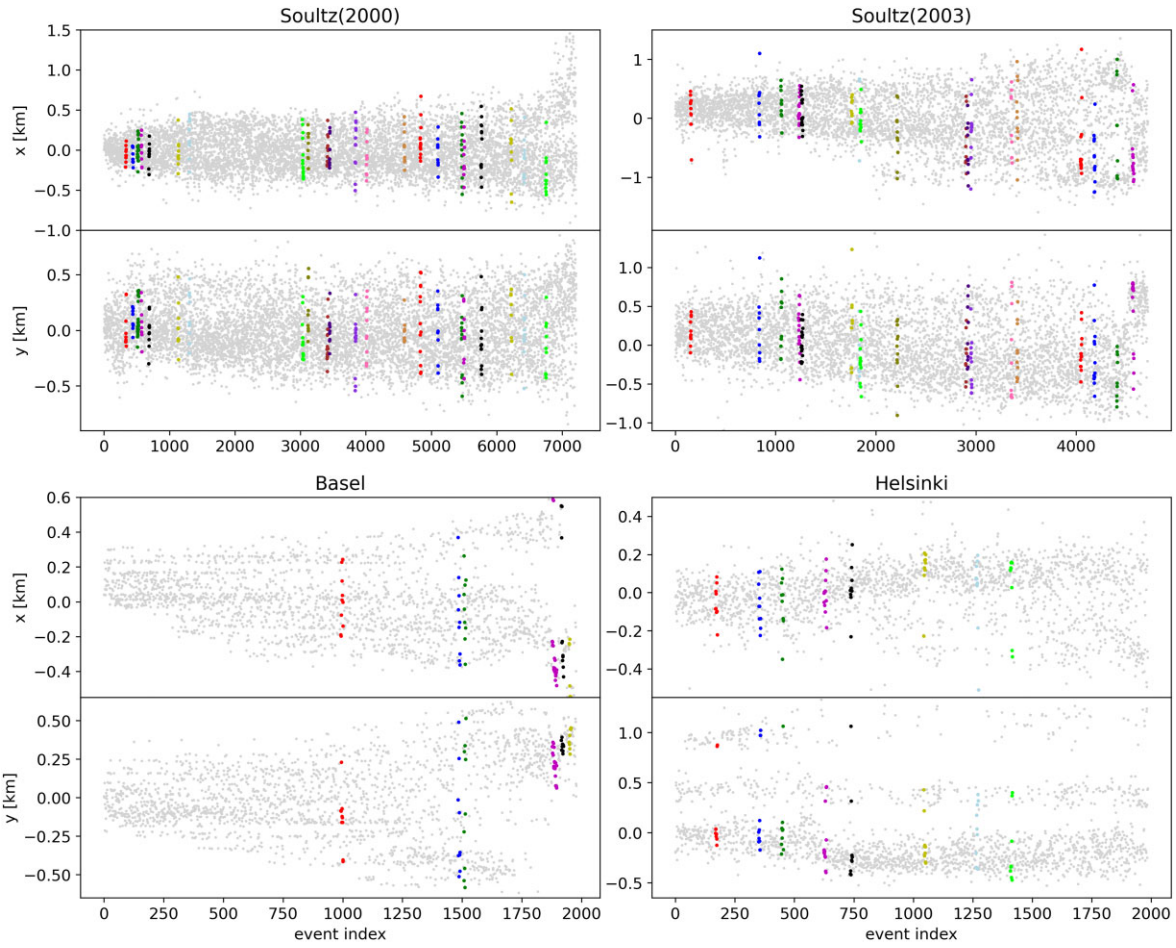

Figure 5. The same as Fig. 4 but for the identified episodes in the injection-induced seismicity cases. The time dependence of the coordinates (x–t plots) is shown in Supplementary Fig. S2.

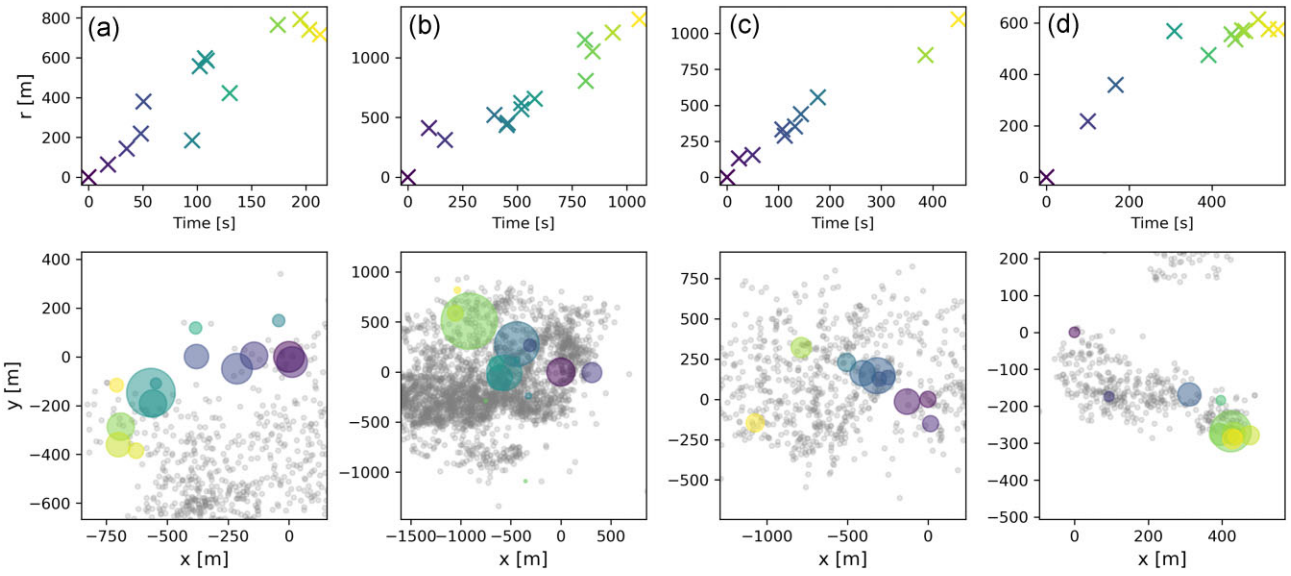

Figure 6. Four examples of identified episodes: (a) the 23th episode of West Bohemia (2000), (b) 25th episode of West Bohemia (2008), (c) 7th episode of West Bohemia (2018) and (d) 2th episode of LongValleyCaldera. In all cases, the upper plot shows the 3-D distance to the first event as function of time, while the bottom plot shows the hypocentre projections on the fault plane where circle size is related to a stress drop of 0.05 MPa and colours refer to the timing indicated in (a). Grey dots refer to the preceding activity in the swarms.

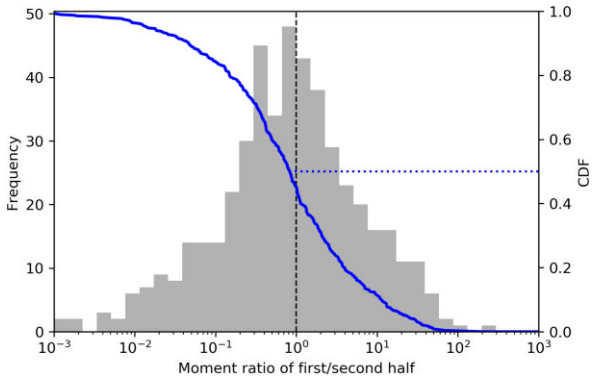

Figure 7. Histogram of the ratio between the seismic moment released by the first and second half of the events in a a detected episode. Additionally, the cumulative distribution function is shown by the blue curve with the scale on the right-hand side. The distribution is approximately symmetric around the ratio of 1.0, indicating their swarm-type character.

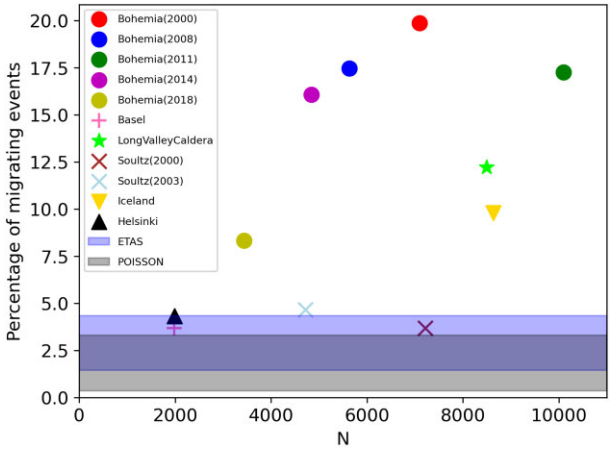

Figure 8. The fraction of migrating events within the sequences. The horizontal bars refer to the range between the 5 per cent and 95 per cent quantiles of the results for synthetic Poisson and ETAS sequences with 5000 events.

between 2000 and 2018, while intermediate values of 12 per cent and 19 per cent are observed for the Long Valley Caldera and Iceland swarms, respectively. These values are larger than the corresponding values in the random Poisson and ETAS sequences by a factor of 3 to 10. In Poisson simulations, the percentage of detected migrating events scatters around 2 per cent, while it scatters around 3 per cent in the case of the ETAS simulations. In contrast to natural swarm activity, such migration patterns are rarely detected in the injection-induced seismicity, where the ratio is within or only slightly above the values in the Poisson and ETAS simulations. Similar results are found for the same analysis restricted to events above the completeness magnitude, as shown in Supplementary Fig. 7.

4.3.2 How do clusters grow in time?

The spatial growth of the identified clustered events with time is unclear because our detection algorithm does not imply any functional dependence on time. Indeed, the detection algorithm involves only the earthquake index and the distance rank, so it is not necessarily expected that the distances of the detected events follow a clear pattern as a function of time. To analyse the growth pattern in a compact way, we measured the distances and times relative to the first event in each episode and stacked all of them in one plot. The result is provided in Fig. 9(a), showing a scattered point cloud spanning a timescale from seconds to tens of days and distances from metres to kilometres. To account for different cluster growth rates, we fitted to each migration episode a linear function $f(t) = vt$ and a square-root function $\sqrt{4\pi Dt}$ and measure the variance reduction $R^2 = 1 - \sum_i [r_i - f(t_i)]^2 / \sum_i [r_i - \bar{r}]^2$, where $\bar{r}$ refers to the mean distance. While a value of $R^2 \leq 0$ would indicate that the data cannot be described at all by a linear or square-root growth function f, a value of $R^2 = 1$ would refer to the perfect fit $r_i = f(t_i)$ for all cluster members. Then we plotted the observed distance versus the rescaled time, either vt in panel Fig. 9(b) or $\sqrt{4\pi Dt}$ in panel Fig. 9(d), using the optimized values v and D for each episode. For earthquakes all triggered at the rupture front position $f(t)$, all points will fall on the diagonal indicated by the dashed red line in Figs 9(b) and (d). The observed points scatter around this line, showing that they follow systematic temporal trends on average. The square-root function fits the majority of the sequences better than the linear function, namely in 60 per cent of the cases. The variance reduction R^2 for the individual episodes is in both cases larger than 50 per cent for most of the episodes, namely in 66 per cent (58 per cent) of the episodes for the square-root (linear) function. The estimated v and D values are shown in Figs 9(c) and (e). The migration velocities range between 0.01 and 10 m s^{-1} for most cases, with a mean value of 1.8 m s^{-1}. The estimated D-values range between 0.1 and 1000 m^2 s^{-1} with a mean of 178 m^2 s^{-1}. Similar values are obtained for the migration episodes detected using a magnitude cutoff, see Supplementary Fig. 8. For pore-pressure diffusion in intact rock, the latter values seem to be too large, see for example Talwani *et al.* (2007) who reported diffusivity of seismogenic fractures not exceeding 10 m^2 s^{-1}. However, if pore-pressure diffusion occurs within a freshly ruptured fault segment, permeability might be strongly increased due to precursory cracking, possibly explaining those high values.

4.3.3 How is the migration velocity related to the episode's duration?

The relation between the mean migration velocity and the duration of the sequences might be indicative of the underlying process. To analyse this relation, we used the velocity values v estimated by the fit of $v \cdot t$ to the time–distance points (t_i, r_i) for each episode, see Fig. 9(a). The duration T is simply determined by the time difference between a episodes's last and first earthquakes. Fig. 10 shows a strong anticorrelation between both values. The linear correlation coefficient between the logarithmic values in Fig. 10 is −0.93. This result indicates that the episodes stop after reaching a similar size independent of the migration speed. The mean value of the product $v \cdot T$ is 1.6 km with [0.4, 2.6] km being the 90 per cent confidence interval. Excluding the Iceland data, the mean is 1.2 km with a confidence interval [0.4, 2.1] km. Similar results are found for the same analysis restricted to events above the completeness magnitude (see Supplementary Fig. 10).

5 THE MOMENT-AREA GROWTH

According to our models of self-driven seismicity, the area occupied by the earthquakes is related to the seismic moment of the events. To analyse this relation for the detected episodes, we first projected the hypocentres to the best-fitting plane and then measured the activated area by its convex hull. For the third and all following events, we calculated the corresponding area A_i and the cumulative seismic moment $M_{0,i}^T$ released until this event during the episode using eq. (5a) for the *crack* and eq. (5b) for the *front model*. For each episode, we then fitted eq. (4) to the points $(A_i, M_{0,i}^T)$ to estimate

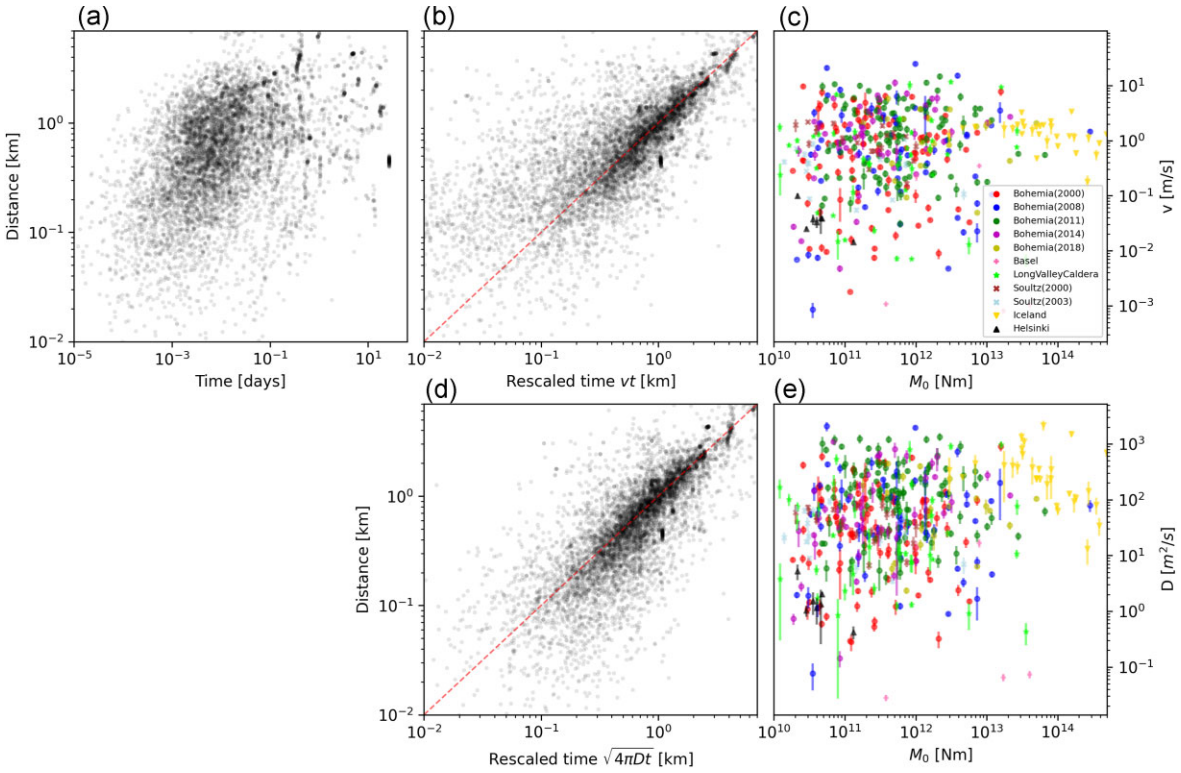

Figure 9. (a) Distance r versus time t of all events ($N = 7725$) in the 480 detected migration episodes, where times and distances are measured relatively to the first event in each sequence. (b) and (d) show the same for rescaled time by the estimated velocity v in the case of linear fits (b) or $\sqrt{4\pi\, Dt}$ in the case of square-root fits (d). Plots (c) and (e) show the estimated propagation velocity (c) and diffusivity (e) as a function of the cumulative seismic moment released during the episodes. In (c) and (e), the error bars refer to one standard deviation. The variance reduction of the corresponding fits is larger than 50 per cent for 58 per cent (66 per cent) of the sequences in the case of linear (square-root) fits, and 60 per cent of the sequences are better fitted by $\sqrt{4\pi\, Dt}$ than vt.

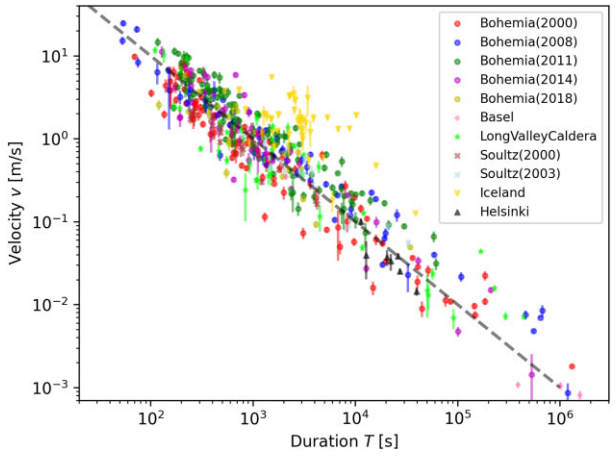

Figure 10. Estimated propagation velocity v as a function of the duration T of the episode. The error bars refer to one standard deviation. The dashed line refers to $v = 1000/T$ [m s^{-1}], indicating that the episodes migrate approximately all the same distance but with different velocities.

the stress drop σ. In Figs 11 (a) and (d) we stack the estimated area versus the calculated M_0^T-values during the cluster evolution of all sequences; each point represents the $M_{0,i}^T$–A_i pair. The large scatter of this plot is likely a result of strongly varying stress drops for different episodes. To account for this, the values of seismic moment and area for each sequence were fitted by eq. (4) providing an estimate of the corresponding stress drop values $\Delta\sigma$. Seismic moments were then rescaled by the stress drops of individual episodes showing much smaller scatter (Figs 11b and e) pointing to clusters' growths in agreement with the model predictions.

Additionally, we calculated the corresponding variance reduction R^2 for each fit. For 42 per cent of the *crack model* fits, and 59 per cent of the *front model* fits more than 50 per cent variance reduction was achieved. The *front model* outperforms the *crack model* in most cases, namely in 94 per cent of the episodes. The estimated stress drops scatter mainly in the range between 100 Pa and 1 MPa (Figs 11c and f), with a slightly larger mean value of 0.3 MPa in the case of the *front model* compared to 0.2 MPa for the *crack model*. Supplementary Fig. S9 provides the similar results obtained for the corresponding analysis restricted to events above the completeness magnitude.

6 DISCUSSION

We find that the fast migration episodes frequently occur during natural earthquake swarms but are quite rare in the analysed injection-induced earthquake activity. Our observation points to possible differences in the underlying triggering process of both seismicity types. It turned out that main shocks do not simply drive those fast migrating episodes, and different driving mechanisms should be sought. Traditionally, both fluid flow and elastic stress transfer are considered responsible for swarms' migration. Stress transfer was found effective in triggering fast sub-sequences of the 2000 West Bohemia swarm (Fischer & Horálek 2005) thanks to elevated pore pressure in the fault zone. For the same swarm, Hainzl & Ogata (2005) found that stress triggering was dominant in driving the observed seismicity, but fluids were needed to initiate and contribute to driving the swarm itself. On the contrary, injection-induced seismicity occurs usually in intact rock or near faults that are not critically stressed.

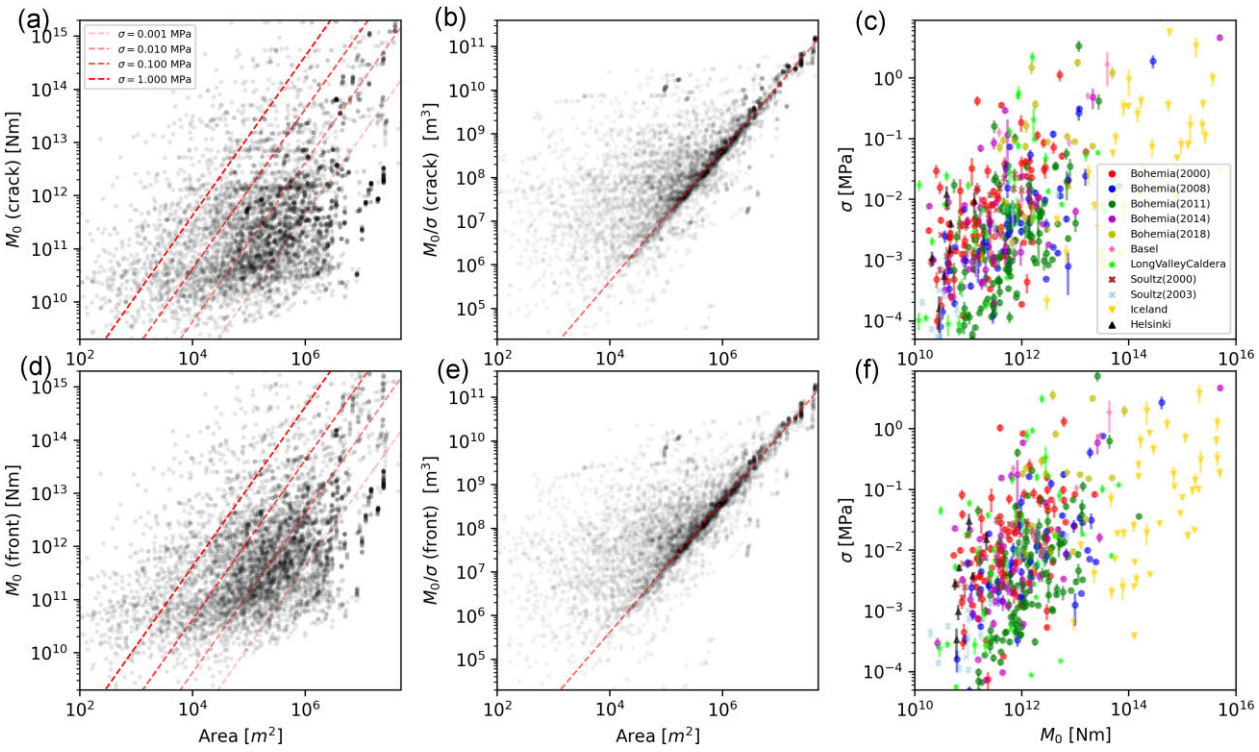

Figure 11. Evolution of the seismic moment release as a function of the area covered on the fault plane and estimated stress drops for the case that seismic moment is measured by eq. (5a) (a–c) or eq. (5b) (d–f). (a) Evolution of the cumulative seismic moment versus covered area on the fault plane, where the dashed red lines refer to the theoretical model lines for stress drops varying from 1 kPa to 1 MPa. (b) and (e) show the same result for seismic moment normalized by the stress drop estimated for the individual migration episodes. The corresponding stress drops are plotted as a function of the total seismic moment release for each episode in panels (c) and (f) for the *crack* and *front model*, respectively, where the error bars refer to one standard deviation.

Another candidate for producing bursts of events manifested by fast hypocentre migration is the aseismic slip supported by pore pressure buildup in the fault zone which could generate the required stress perturbations (Lohman & McGuire 2007; De Barros *et al.* 2020; Dublanchet & De Barros 2020). This could be the reason for the less frequent occurrence of fast migration episodes in seismicity induced by fluid injections, which are usually not performed along faults and so the slow slip is less likely in these cases. Indeed, injection-induced swarms are understood as a response of the rock medium to an anthropogenic pore pressure perturbation in otherwise stable areas with no aseismic slip.

Although the migration episodes were detected without time information, most of them form systematic trends in time, either showing linear or square-root growth. In particular, the square-root function fits better with 66 per cent of the episodes showing more than 50 per cent variance reduction compared to 58 per cent of the episodes for the linear fit (Fig 9d). The increase of the cumulative seismic moment release as a function of the rupture area growth is best explained by the *front model* (Fig 11b). Both observations indicate a sectorial front growth (illustrated in Fig. 3c) with decreasing rupture speed. The square-root rupture speed could indicate that pore pressure diffusion drives the activity. However, it should be noted that a square-root migration is also observed for slow slip events (Ide 2010) and the square-root growth is similarly explained by 2-D hydraulic fracture growth, given a constant inflow rate. In this case, the fracture and the associated seismicity is directly driven by the pressurized water flow, which differs from the *front model* where fluid flow is only enabled by the fracture growth.

The propagation velocity of the fast migrating episodes scatters around 1 $m\,s^{-1}$, corresponding to a scatter around approximately 100 $km\,d^{-1}$. This exceeds by approximately one order the velocity of fast migrating episodes in the 2015 Corinth rift swarm (De Barros *et al.* 2020; Dublanchet & De Barros 2020). This difference is possibly not related to the different tectonic environments of the swarms in question but most probably accounts for the differing methods used for episodes detection. While the fast migration episodes in the Corinth rift swarm were detected manually, our results are based on automatically detected episodes; the detection method identifies subsequent events, which could tend to highlight fast migration velocities. It is interesting to note that Danré *et al.* (2022) obtained a similar anticorrelation of migration velocity with swarm duration (fig. 4 in their paper). In their case, the migration velocities range from 1 to 10^4 $m\,d^{-1}$, which is by three orders of magnitude smaller than our migration velocities. The reason is that Danré *et al.* (2022) analysed the average velocity of the seismicity front, which is in principle much smaller than the migration rate of fast episodes within the swarm.

We observe a clear anticorrelation between the estimated cluster growth velocities and the duration of the clusters. This observation means that migration clusters reach, on average, independently of their migration speed, a similar final size. Even more surprisingly, the same relationship is observed for the different swarms, whether they are natural or injection-induced. This points to a dynamic effect of the underlying process, which is not well understood so far. Interestingly, the identified episodes span across the entire activated fault segment; see Figs. 4 and 5. The mean value $v \cdot t$ of 1.6 km points to a typical size of the activated clusters and its maximum size could be related to seismogenic depth of the crust mapped by the maximum hypocentre depth. This ranges from 6–7 km in Long-Valley Caldera and Iceland (Shelly *et al.* 2016; Fischer *et al.* 2022) to about 13 km in West Bohemia (Fischer *et al.* 2014).

In many cases, the migration episodes form spatially continuous clusters (Fig. 6). Spatial discontinuities that appear inconsistent with the *front model* could be related to missing small events or aseismic deformation that do not require continuous event clusters. This is consistent with the rather low stress drops we observe.

Our results show that the relation of the seismic moment and activated area of most sequences can be successfully fitted by the *front* and/or *crack model*. This is apparent in Figs 11(a)–(d) where the scatter of the points significantly decreases when the cumulative seismic moment is scaled by the estimated stress drop and the points align along a line with the slope of 3/2 as predicted by eq. (4). This indicates the fast propagating episodes are driven by the seismic activity itself with fluid flow that follows the fracture growth and supports it from behind.

7 CONCLUSIONS

We analysed the growth of earthquake clusters with the focus to fast migration episodes that are embedded in the overall migration trend and occur mainly during earthquake swarms. The aim of our study was to unveil the physical mechanism responsible for this unique phenomenon. After reviewing the sources of earthquake migration and the ways how to graphically analyse it we propose a simple scheme for distinguishing between the external (aseismic) and internal (seismic) drive of the activity. Next we focus on the self-driven (seismic) mechanism and propose two models, the *crack* and the *front model* that can explain the hypocentre spreading. They are characterized by the binded growth of cumulative seismic moment and activated fault area. It is shown that the relation of these quantities differ for the two models, which allows for identification of the background mechanism.

We developed automatic algorithm for detection of the migration episodes in seismicity data and applied it on relocated catalogues of natural earthquake swarms and injection induced seismicity. It turned out that the fast migration episodes are quite frequent during natural earthquake swarms (8–20 per cent of all events) compared to fluid induced seismicity (less than 5 per cent of the events). We also found that although episodes were detected independently of time, they grew monotonically with time according to a linear or square-root dependence of radius on time; for majority of sequences the square-root growth showed a better fit. A quite high propagation velocity of the episodes migration in the range of 1 m s^{-1} was found; its anticorrelation with the episodes duration points to a similar final cluster size in the range of one to two kilometres.

The comparison of the growth of seismic moment and the activated fault area with the proposed models shows that both the rupture *front model* and *crack model* are able to explain the observed migration, however the *front model* is more consistent with the data. The relatively low estimated stress drops ranging between 100 Pa and 1 MPa indicate that aseismic processes are also in place. Our results show that the fast migrating episodes can be driven by stress transfer between adjacent events with the support of aseismic slip or fluid flow due to dynamic pore creation.

SUPPORTING INFORMATION

Supplementary data are available at *GJI* online.

Figure S1. All identified clusters of the analysed natural swarms (besides the Iceland case), shown as function of time (in contrast to the main text figure, where it is shown as function of the event index).

Figure S2. All identified clusters of the injection experiments, shown as function of time (in contrast to the figure in the main text, where it is shown as function of the event index).

Figure S3. Same as the main text Fig. 3 but using magnitude cutoffs defined by the maximum curvature method.

Figure S4. Same as the main text Fig. 4 but using magnitude cutoffs defined by the maximum curvature method.

Figure S5. Clusters selected with magnitude cutoff based on the maximum curvature method: Four examples of identified clusters: (a, b) third and 18th cluster of West Bohemia (2000), (c) 8th cluster of West Bohemia (2008), (c) 21th cluster of West Bohemia (2008), and (d) 4th cluster of West Bohemia (2018). In all cases, the upper plot shows the 3-D distance to the first event as function of time, while the bottom plot shows the hypocentre projections on the fault plane where circle size is related to a stress drop of 0.05 MPa and colours refer to the timing indicated in (a). The grey dots refer to the preceding activity in the swarms.

Figure S6. Clusters selected with magnitude cutoff: Histogram of the ratio of seismic moment released per event in the first half events in a cluster to the mean moment released by the second half events. Additionally, the cumulative distribution function is shown by the blue curve with the scale on the right. The distribution is approximately symmetric around the ratio of 1.0, indicating their swarm-type character.

Figure S7. Clusters selected with magnitude cutoff: The fraction of migrating events within the sequences. The horizontal bars refer to the range between the 5 per cent and 95 per cent quantiles of the results for synthetic Poisson and ETAS sequences with 5000 events.

Figure S8. Clusters selected with magnitude cutoff: (a) Stacked distance r versus time t of all clustered events ($N = 6665$) in the 370 detected migration clusters, where times and distances are measured relative to the first event in each sequence. (b) and (d) show the same for rescaled time by the estimated velocity v in the case of linear fits (b) or $\sqrt{4\pi\, Dt}$ in the case of square-root fits (d). Plots (c) and (e) show the estimated propagation velocity (c) and diffusivity (e) as a function of the cumulative seismic moment of the clusters. In (c) and (e), the error bars refer to one standard deviation. The variance reduction of the corresponding fits is larger than 50 per cent for 60 per cent (68 per cent) of the sequences in the case of linear (square-root) fits, and 59 per cent of the sequences are better fitted by $\sqrt{4\pi\, Dt}$ than vt.

Figure S9. Clusters selected with magnitude cutoff: Evolution of the seismic moment release as a function of the area covered on the fault plane and estimated stress drops for the case that seismic moment is measured by eq. (5) (a–c) or eq. (6) (d–f). (a) Evolution of the cumulative seismic moment versus covered area on the fault plane, where the dashed red lines refer to the theoretical model lines for stress drops varying from 1 kPa to 1 MPa. (b) and (e) show the same result for seismic moment normalized by the stress drop estimated for the individual clusters. The corresponding stress drops are plotted as a function of the total seismic moment release for each cluster in panels (c) and (f) for the crack and front model, respectively, where the error bars refer to one standard deviation.

Figure S10. Clusters selected with magnitude cutoff: Estimated propagation velocity v as a function of the duration T of the clusters. The dashed line refer to $v = 1000/T$ [m s^{-1}], indicating that the cluster migrate approximately all the same distance but with different velocities.

Please note: Oxford University Press is not responsible for the content or functionality of any supporting materials supplied by the authors. Any queries (other than missing material) should be directed to the corresponding author for the paper.

ACKNOWLEDGMENTS

The work of TF and JV was supported by the Czech Funding Agency under the grant 20-26018S.

DATA AVAILABILITY STATEMENT

The data underlying this article will be shared on request to the corresponding author.

REFERENCES

Bachura, M., Fischer, T., Doubravová, J. & Horálek, J., 2021. From earthquake swarm to a mainshock-aftershocks: the 2018 activity in West Bohemia/Vogtland, *Geophys. J. Int.,* **224,** 1835–1848.

Charléty, J., Cuenot, N., Dorbath, L., Dorbath, C., Haessler, H. & Frogneux, M., 2007. Large earthquakes during hydraulic stimulations at the geothermal site of Soultz-sous-Forêts, *Int. J. Rock Mech. Min. Sci.,* **44**(8), 1091–1105.

Danré, P., De Barros, L., Cappa, F. & Ampuero, J.-P., 2022. Prevalence of aseismic slip linking fluid injection to natural and anthropogenic seismic swarms, *J. geophys. Res.: Solid Earth,* **127,** e2022JB025571, doi:10.1029/2022JB025571.

De Barros, L., Cappa, F., Deschamps, A. & Dublanchet, P., 2020. Imbricated aseismic slip and fluid diffusion drive a seismic swarm in the Corinth Gulf, Greece, *Geophys. Res. Lett.,* **47,** e2020GL087142, doi:10.1029/2020GL087142.

De Barros, L., Wynants-Morel, N., Cappa, F. & Danre, P., 2021. Migration of fluid-induced seismicity reveals the seismogenic state of faults, *J. geophys. Res.: Solid Earth,* **126,** e2021JB022767, doi:10.1029/2021JB022767.

Dublanchet, P. & De Barros, L., 2020. Dual seismic migration velocities in seismic swarms, *Geophys. Res. Lett.,* **47,** e2020GL090025, doi:10.1029/2020GL090025.

Fischer, T. & Hainzl, S., 2017. Effective stress drop of earthquake clusters, *Bull. seism. Soc. Am.,* **107,** 2247–2257.

Fischer, T. & Hainzl, S., 2021. The Growth of Earthquake Clusters, *Front. Earth Sci.,* **9,** 638336 , doi:10.3389/feart.2021.638336.

Fischer, T., Hainzl, S. & Dahm, T., 2009. Asymmetric hydraulic fracture as a result of driving stress gradients, *Geophys. J. Int.,* **179,** 634–639.

Fischer, T., Hainzl, S., Eisner, L., Shapiro, S.A. & Le Calvez, J., 2008. Microseismic signatures of hydraulic fracture growth in sediment formations: observations and modeling, *J. geophys. Res.: Solid Earth,* **113,** B02307, doi:10.1029/2007JB005070.

Fischer, T. & Horálek, J., 2005. Slip-generated patterns of swarm microearthquakes from West Bohemia/Vogtland (central Europe): evidence of their triggering mechanism?, *J. geophys. Res.: Solid Earth,* **110,** B05S21 , doi:10.1029/ 2004JB003363.

Fischer, T., Horálek, J., Hrubcová, P., Vavrycuk, V., Brauer, K. & Kampf, H., 2014. Intra-continental earthquake swarms in West-Bohemia and Vogtland: a review, *Tectonophysics,* **611,** 1–27.

Fischer, T., Hrubcová, P., Salama, A., Doubravová, J., Ágústsdóttir, T., Gudnason, E.Á., Horálek, J. & Hersir, G.P., 2022. Swarm seismicity illuminates stress transfer prior to the 2021 Fagradalsfjall eruption in Iceland, *Earth planet. Sci. Lett.,* **594,** 1117685 , doi:10.1016/j.epsl.2022.117685.

Ghosh, A., Vidale, J.E., Sweet, J.R., Creager, K.C., Wech, A.G., Houston, H. & Brodsky, E.E., 2010. Rapid, continuous streaking of tremor in Cascadia, *Geochem. Geophys. Geosyst.,* **11,** Q12010 , doi:10.1029/2010GC003305.

Gombert, B. & Hawthorne, J. C., 2023. Rapid tremor migration during few minute-long slow earthquakes in Cascadia, *J. geophys. Res.: Solid Earth,* **128,** e2022JB025034.

Guo, Y., Zhuang, J. & Zhang, H., 2023. Detection and characterization of earthquake swarms in Nankai and its association with slow slip events, *J. geophys. Res.: Solid Earth,* **128,** e2022JB025984, doi:10.1029/2022JB025984.

Hainzl, S. & Fischer, T., 2002. Indications for a successively triggered rupture growth underlying the 2000 earthquake swarm in Vogtland/NW Bohemia, *J. geophys. Res.: Solid Earth,* **107,** 2338 , doi:1029/2002JB001865.

Hainzl, S. & Ogata, Y., 2005. Detecting fluid signals in seismicity data through statistical earthquake modeling, *J. geophys. Res.: Solid Earth,* **110,** B05S07 , doi:10.1029/2004JB003247.

Heaton, T.H., 1990. Evidence for and implications of self-healing pulses of slip in earthquake rupture, *Phys. Earth planet. Inter.,* **64,** 1–20.

Ide, S., 2010. Striations, duration, migration and tidal response in deep tremor, *Nature,* **466,** 356–360.

Jaeger, J., 1951. *An Introduction to Applied Mathematics,* pp. 364–369, Clarendon Press.

Kapetanidis, V., Deschamps, A. *et al.*, 2015. The 2013 earthquake swarm in Helike, Greece: seismic activity at the root of old normal faults, *Geophys. J. Int.,* **202,** 2044–2073.

Kraft, T. & Deichmann, N., 2014. High-precision relocation and focal mechanism of the injection-induced seismicity at the Basel EGS, *Geothermics,* **52,** 59–73.

Kwiatek, G., Martínez-Garzón, P., Davidsen, J., Malin, P., Karjalainen, A., Bohnhoff, M. & Dresen, G., 2022a. Limited earthquake interaction during a geothermal hydraulic stimulation in Helsinki, Finland, *J. geophys. Res.: Solid Earth,* **127,** e2022JB024354 , doi:10.1029/2022JB024354.

Kwiatek, G., Martínez-Garzón, P. & Karjalainen, A. 2022b. *Earthquake catalog of induced seismicity associated with 2020 hydraulic stimulation campaign at OTN-2 well in Helsinki,* GFZ Data Services, Finland. https://doi.org/10.5880/GFZ.4.2.2022.001.

Lohman, R.B. & McGuire, J.J., 2007. Earthquake swarms driven by aseismic creep in the Salton Trough, California, *J. geophys. Res.: Solid Earth,* **112,** B04405 , doi:10.1029/2006JB004596.

Madariaga, R. & Ruiz, S., 2016. Earthquake dynamics on circular faults: a review 1970-2015, *J. Seismol.,* **20,** 1235–1252.

Marone, C., Raleigh, C. B. & Scholz, C. H., 1990. Frictional behavior and constitute modeling of simulated fault gouge, *J. geophys. Res.: Solid Earth,* **95,** 7007–7025.

Massin, F., Farrell, J. & Smith, R.B., 2013. Repeating earthquakes in the yellowstone volcanic field: implications for rupture dynamics, ground deformation, and migration in earthquake swarms, *J. Volc. Geotherm. Res.,* **257,** 159–173.

McGarr, A., 2014. Maximum magnitude earthquakes induced by fluid injection, *J. geophys. Res.,* **119,** 1008–1019.

Ogata, Y., 1998. Space-time point-process models for earthquake occurrence, *Ann. Inst. Stat. Math.,* **50,** 379–402.

Parotidis, M., Rothert, E. & Shapiro, S.A., 2003. Pore-pressure diffusion: a possible triggering mechanism for the earthquake swarms 2000 in Vogtland/NW-Bohemia, central Europe, *Geophys. Res. Lett.,* **30**(20), 2075, doi:10.1029/2003GL018110.

Passarelli, L., Selvadurai, P. A., Rivalta, E. & Jónsson, S., 2021. The source scaling and seismic productivity of slow slip transients, *Sci. Adv.,* **7,** eabg9718.

Rundle, J.B., Luginbuhl, M., Giguere, A. & Turcotte, D.L., 2018. Natural time, nowcasting and the physics of earthquakes: estimation of seismic risk to global megacities, *Pure appl. Geophys.,* **175,** 647–660.

Shapiro, S.A., Huenges, E. & Borm, G., 1997. Estimating the crust permeability from fluid-injection-induced seismic emission at the KTB site, *Geophys. J. Int.,* **131,** F15–F18.

Shelly, D. R., Ellsworth, W. L. & Hill, D. P., 2016. Fluid-faulting evolution in high definition: connecting fault structure and frequency-magnitude variations during the 2014 Long Valley Caldera, California, earthquake swarm, *J. geophys. Res.: Solid Earth,* **121**(3), 1776–1795.

Shelly, D.R. & Hill, D.P., 2011. Migrating swarms of brittle-failure earthquakes in the lower crust beneath Mammoth Mountain, California, *Geophys. Res. Lett.,* **38,** L20307.

Talwani, P., Chen, L. & Gahalaut, K., 2007. Seismogenic permeability, k_s, *J. geophys. Res.: Solid Earth,* **112,** B07309, doi: 10.1029/2006JB004665.

Wells, D.L. & Coppersmith, K.J., 1994. New empirical relationships between magnitude, rupture length, rupture width, rupture area, and surface displacement, *Bull. seism. Soc. Am.,* **84,** 974–1002.

Woods, J., Winder, T., White, R.S. & Brandsdóttir, B., 2019. Evolution of a lateral dike intrusion revealed by relatively-relocated dike-induced earthquakes: the 2014-15 Bárdarbunga-Holuhraun rifting event, Iceland, *Earth planet. Sci. Lett.*, **506,** 53–63.

Wright, T.J. *et al.*, 2012. Geophysical constraints on the dynamics of spreading centres from rifting episodes on land, *Nat. Geosci.*, **5,** 242, doi:10.1038/NGEO1428.

Yamashita, T., 1999. Pore creation due to fault slip in a fluid-permeated fault zone and its effect on seismicity: generation mechanism of earthquake swarm, *Pure appl. Geophys.*, **155,** 625–647.

Yoshida, K. & Hasegawa, A., 2018a. Hypocenter migration and seismicity pattern change in the Yamagata–Fukushima border, NE Japan, caused by fluid movement and pore pressure variation, *J. geophys. Res.: Solid Earth,* **123,** 5000–5017.

Yoshida, K. & Hasegawa, A., 2018b. Sendai-Okura earthquake swarm induced by the 2011 Tohoku-Oki earthquake in the stress shadow of NE Japan: detailed fault structure and hypocenter migration, *Tectonophysics,* **733,** 132–147.

APPENDIX A: DETECTION ALGORITHM

The detection algorithm is based on the distances' rank variability of subsequent events. By its construction, the algorithm does not make any assumptions of the specific space–time relations of the underlying process. In particular, the discriminator variable D_V for a sequence of distances $r_i (i = 1, \ldots, N)$ is calculated by

(i) first calculating the rank$_i$ of each value r_i, where, for example the smallest r gets rank=1 and the largest r gets rank $= N$ and

(ii) secondly determining the standard deviation σ_Δ of the difference between subsequent ranks, $\Delta_i = \text{rank}_{i+1} - \text{rank}_i$, with $i = 1, \ldots, N-1$.

The discriminator is then defined by $D_V = \sigma_\Delta/(N-1)$. Its calculation is illustrated in Fig. A1.

The full earthquake activity is scanned by this discriminator value to detect migration patterns. In particular, for a chronologically ordered sequence of hypocentres $\vec{x}_i$ (related to $i = 1, \ldots, Z$ earthquakes with magnitudes $m_i \geq M_c$), the following algorithm is used to detect migration patterns within this sequence according the following steps:

(i) We set the minimum sequence length to $N_{\min} = 10$ and the detection threshold to $D_{V,\min} = 0.2$, which is well below the confidence interval of random data (see Fig. A2).

(ii) Set $i = 1$

(iii) Calculate the distance r of all subsequent events relative to location $\vec{x}_i$ ($Z - i$ values) and determine the corresponding $D_V(k)$ for the first k values, with $N_{\min} \leq k < Z$.

(iv) Determine the maximum D_V and its k-value, $D_{V,i}, k_i$. If $D_{V,i} \leq D_{V,\min}$, all events $i+1, \ldots, i+k_i$ are connect to the migration pattern starting with event i.

(v) If $i < Z - N_{\min}$, set $i = i + 1$ and repeat steps 3 and 4

(vi) Merge migration sequences: All subsequent events which belong to any individual migration pattern are grouped together. A grouped cluster ends when the next event does not belong to any sequence.

(vii) Condense each merged cluster by choosing the most significant subsequence: Follow steps 2–6 for each cluster and finally replace the cluster by the subsequence with maximum D_V-value.

The algorithm is tested for synthetic data with nested linear hypocentre growth (in two dimensions) within stationary seismicity before and afterwards. The migrating of distance $R = 10$ with N events is simulated for a period of 50 by a unilateral moving Gaussian distribution with velocity $v = 0.2$ and standard deviation of σ_x.

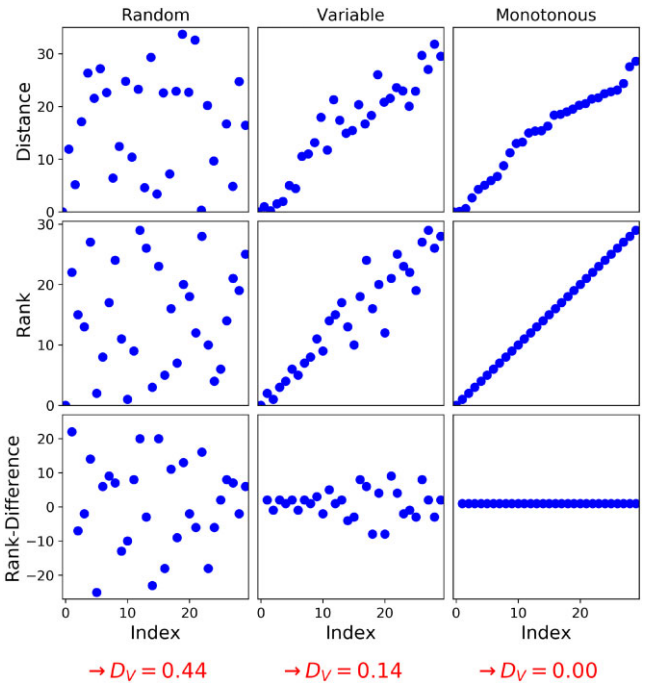

Figure A1. Three examples (columns) to demonstrate the steps (from top to bottom) for calculation of the discriminator value D_V.

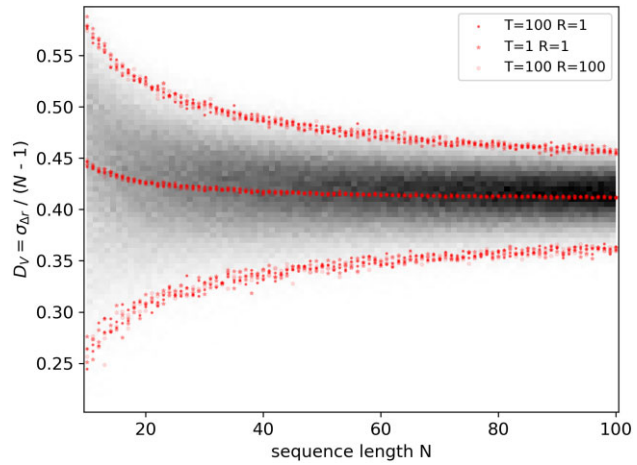

Figure A2. Colour-coded density of D_V values as function of the sequence length N for randomly distributed 2-D event data. The mean and the 1 per cent and 99 per cent percentiles of the D_V value for a Gaussian, respectively uniform, distribution and the three different T–R parameter sets are marked by symbols.

Note that the larger σ_x, the greater the scatter around the migration trend, and that the spatial and temporal scales are dimensionless and can be rescaled to any value. One example with $N = 50$ and $\sigma_x = 1.0$ is presented in Fig. A3(a), while a systematic analysis for different values of N and σ_x is shown in Fig. A3(b). The algorithm is found to work for these synthetics appropriately if the ratio, σ_x/R, between variability/uncertainty and the final extension is smaller than approximately 20 per cent, that is $\sigma_x < 2$.

The rate of false detections can be evaluated based on the random simulations described in Section 4.3.1 with results presented in Fig. 8. In the case of randomly distributed events in a box, on average 2 per cent of the events are falsely identified as part of a migration episode.

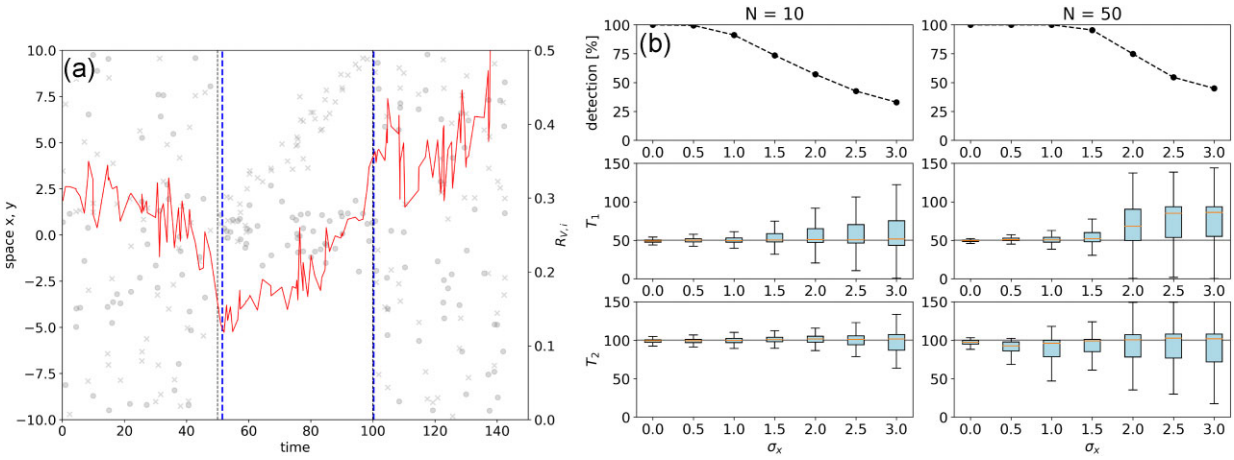

Figure A3. (a) Example synthetic sequence with an embedded linear growth ($\sigma_x = 1.0$) consisting of $N = 50$ events: Event locations x (crosses) and y (circles) with scale on left and D_V value (scale on right) as a function of time. Vertical black lines mark the true migration period, while the vertical blue lines refer to the identified onset time T_1, the end time T_2. (b) Results for 1000 synthetic sequences for embedded migration episodes with different N (columns) and different variability σ_x shown in each x-scale. The first row provides the percentage of sequences in which a migration pattern is identified by the algorithm. The following rows show the estimated onset T_1 and the end T_2 for the detected cases.

APPENDIX B: SYNTHETIC SIMULATIONS

B1 Migrating events

For illustration, we used in Section 2.2 synthetic sequences, which were simulated according to the following algorithms.

B1.1 Events triggered by pore-pressure diffusion

For simplicity, we consider a 1-D pore-pressure diffusion with a step-function boundary condition (Jaeger 1951)

$$p(r, t) = p_0 \left[1 - \mathrm{Erf}\left(\frac{r}{2\sqrt{Dt}}\right)\right], \tag{B1}$$

where both values, the boundary pressure p_0 and the hydraulic diffusivity D, are set to one. Asperities are uniformly distributed in space, and their initial stress values are uniformly distributed below the critical failure stress. The stress increases by p according to eq. (B1) with time at the location r of the asperities. The simulated sequence finally consists of the failure times and distances of the asperities.

B1.2 Self-driven front migration

In this case, we consider a channel with width $W = 100$ m, which is successively ruptured by subsequent earthquakes nucleating at the tip of each other. In particular, the position of the rupture front increases with each earthquake according to $\Delta r = A/W$, where the event's rupture area A is calculated based on eq. (1) with stress drop of 1 MPa and an earthquake's magnitude randomly selected from a Gutenberg–Richter distribution in the magnitude range [0, 3] with $b = 1$. The interevent-times Δt are taken from a power-law distribution $\sim(c + \Delta t)^{-p}$ with $p = 1.4$ according to the empirical observations for West Bohemian swarms (Hainzl & Fischer 2002).

B2 Poisson and ETAS simulations

Each Poisson simulation consists of 5000 events uniformly distributed within a box with a 5 km × 5 km dimension.

To be more realistic, we also run simulations of the Epidemic Type Aftershock Sequence (ETAS) model (Ogata 1998), which considers, in addition to randomly distributed background activity, aftershock triggering following empirical relations, specifically the Omori-Utsu decay of the aftershock rates with time, the exponential increase of the aftershock productivity with main shock magnitude, and the power-law type decay of the aftershock density with distance.

Similarly to the Poisson synthetics, each simulation consists of 5000 events in total, initiated by a background rate of 100 events per day in a 5 km × 5 km box, and simulated earthquake magnitudes according to the Gutenberg-Richter distribution in the magnitude range between 0 and 5 with a b-value of one. For aftershock triggering, we use standard parameters. First, we use $c = 0.01$ d and $p = 1.2$ for the temporal decay as a function of time t after the main shock according to $(c + t)^{-p}$. Secondly, we set $K = 0.055$ and $\alpha = 1.0$ for the aftershock productivity as a function of the main shock magnitude m according to $K \cdot 10^{\alpha m}$, which leads to a branching parameter of 0.8, that is, 80 per cent aftershocks on average. Thirdly, the spatial probability density function $(1 - q)/(\pi d^2)(1 + r^2/d^2)^{-q}$ is used with $q = 1.5$ and $d = 0.013 \cdot 10^{-0.5m}$ which equals the scaling of the subsurface rupture length for normal faulting (Wells & Coppersmith 1994).